

RESEARCH ARTICLE

Wind turbine boundary layer arrays for Cartesian and staggered configurations-Part I, flow field and power measurements

Nicholas Hamilton, Matthew Melius and Raúl Bayoán Cal

Department of Mechanical and Materials Engineering, Portland State University, PO Box 751, Portland, Oregon 97207-0751, USA

ABSTRACT

Model wind turbine arrays were developed for the purpose of investigating the wake interaction and turbine canopy layer in a standard cartesian and row-offset turbine array configurations. Stereographic particle image velocimetry was used to collect flow data upstream and downstream of entrance and exit row turbines in each configuration. Wakes for all cases were analyzed for energy content and recovery behavior including entrainment of high-momentum flow from above the turbine canopy layer. The row-offset arrangement of turbines within an array grants an increase in streamwise spacing of devices and allows for greater wake remediation between successive rows. These effects are seen in exit row turbine wakes as changes to statistical quantities including the in-plane Reynolds stress, $-\bar{uv}$, and the production of turbulence. The recovery of wakes also strongly mitigates the perceived underperformance of wind turbines within an array. The flux of kinetic energy is demonstrated to be more localized in the entrance rows and in the offset arrangement. Extreme values for the flux of kinetic energy are about 7.5% less in the exit row of the cartesian arrangement than in the offset arrangement. Measurements of mechanical torque at entrance and exit row turbines lead to curves of power coefficient and demonstrate an increase in efficiency in row-offset configurations. Copyright © 2014 John Wiley & Sons, Ltd.

KEYWORDS

atmospheric boundary layer; wind turbine array; wake recovery; turbulence

Correspondence

Raúl Bayoán Cal, Department of Mechanical and Materials Engineering, Portland State University, PO Box 751, Portland, Oregon 97207-0751, USA.

E-mail: cal@me.pdx.edu

Received 15 April 2013; Revised 30 September 2013; Accepted 4 November 2013

1. INTRODUCTION

Wind turbines and their wakes have been studied to some extent on an individual basis.^{1–3} A review of aerodynamic considerations in turbine design and analysis is presented in the work by Snel.⁴ The combined effects of wake-dynamic interaction within the turbine canopy, however, is still a matter of study. Wind turbine arrays have been modelled numerically as in the studies by Barthelmie *et al.*, Crespo *et al.*, Frandsen *et al.* and Rathmann *et al.*^{5–8} Many of the current models use velocity deficit profiles obtained from experimental and theoretical work. The growth rate of wakes in turbine arrays are generally determined as being caused by the ambient turbulence, which is in turn produced by the shear in the wake from the turbine itself. Generally, the magnitude of the maximum velocity deficit in the wakes is obtained from global momentum conservation.

The wind turbine array has been optimized in the sense of spacing of component turbines to maximize efficiency as in the work by Meyers and Meneveau.⁹ Large wind farms have been shown to increase the effective surface roughness for the atmospheric boundary layer (ABL) and decreasing the wind velocity at turbine-hub height when compared with an otherwise undisrupted ABL. Often, increasing the turbine-land area density (i.e., decreasing the average wind-turbine spacing) has an opposing effect on the total extracted power per turbine. The optimization undertaken in the work by Meyers and Meneveau⁹ addresses the problem of wind-turbine spacing in wind farms, where the optimal spacing is a product of economical constraints and the performance of turbines within the array. This study showed that the optimal spacing

for turbines based on performance may be as large as 15 rotor diameters in the streamwise direction rather than the six or seven diameters typically found in real installations.

In the work by Chamorro and Porté-Agel,¹⁰ an experiment was conducted for an individual wind turbine in order to analyze the wake in the ABL. Mean velocity was assessed using hot-wire anemometry in order to characterize the cross-sectional distribution of mean velocity, turbulence intensity and kinematic shear stress. Multiple locations downstream of the turbine were surveyed for two surface roughness cases. The spatial distribution of the velocity deficit and the turbulence intensity, which are important factors affecting turbine power generation and fatigue loads in wind energy parks, were found to exhibit non-axisymmetric behavior. The distribution of turbulence intensity in the wake was found to be stronger over the rougher surfaces, where the incoming flow is less uniform at the turbine level. A similar study was conducted via a large eddy simulation in the work by Wu and Porté-Agel.¹¹ There, the surface roughness was varied and the effects characterized in various turbulence statistics. From the simulation, it was seen that the velocity deficit and the added turbulence intensity in the wake of a single wind turbine relied on the simulated surface roughness.

The near wake of a small horizontal-axis wind turbine over a range of tip speed ratios was assessed in the work by Ebert and Wood.¹² In the study, the formation and development of the three-dimensional near-wake was measured at six axial locations within two chord lengths of the blades. It was found that at the lowest tip speed ratio, the turbulence level in the wake was very high, suggesting separation from the blades, which are operating at high angles of attack. It was also shown that the three-dimensionality did not contribute significantly to the balance of angular momentum in the wake. Ebert and Wood found evidence that by increasing the tip speed ratio, angular momentum that resided in the tip vortices also increased.

Measurement of the flow within wind turbine arrays has been undertaken as in the studies by Chamorro *et al.* and Chamorro and Porté-Agel,^{13,14} where both regularly spaced turbines and row-offset arrangements were characterized. Chamorro and Porté-Agel were able to establish statistical trends for turbulent quantities throughout the entire array and make location-based comparisons of stresses to determine the shape of layers in the ABL and turbine canopy. In these two studies, it was shown that turbulent quantities became independent of location within the wind turbine arrays beyond the fourth or sixth rows for cartesian and row-offset arrays, respectively. These data and experiments are discussed further in Sections 3.3 and 4.

Wind turbines extract kinetic energy from the mean flow in the direction perpendicular to the plane containing the rotor. This energy has been correlated to a difference in the flux of turbulence kinetic energy at top-tip and bottom-tip locations. In large arrays especially, the kinetic energy entrainment is globally downward from the free flow above the wind turbines into the main canopy layer. Optimization of the flux of kinetic energy is a pursuit of those who would push the operating efficiency of wind turbines, individually or in large-scale arrays, toward the theoretical maximum. The formulation of the flux of kinetic energy suggests that energy containing structures, especially those associated with the top tip of the rotor area, are responsible for the entrainment of energy downward into the main turbine canopy area.^{15,16}

Given the understanding that the flux of kinetic energy from above the wind turbine canopy is a major contributor to the remediation of wakes in the ABL, investigation of its component quantities is of continued interest in studies pertaining to wind turbine arrays. Dependence and behavior of the mean streamwise flow and Reynolds shear stresses upon configuration of wind turbines within an array are analyzed in the present study. Direct quantitative comparisons thereof lend insight as to the formulation of the vertical entrainment of high-momentum air from the ABL above the turbine canopy for entrance-row and exit-row wind turbines in an array.

2. THEORY

The Reynolds-averaged Navier–Stokes boundary layer equation in the streamwise direction can be written as shown in Equation (1). Note that the terms involving viscous dissipation and diffusion are omitted here as all measurements are made sufficiently far from solid boundaries to neglect viscous contributions to the local energy balance

$$U_j \frac{\partial U_i}{\partial x_j} = -\frac{1}{\rho} \frac{\partial P}{\partial x_i} - \frac{\partial \bar{u}_i \bar{u}_j}{\partial x_j} - \bar{f}_i. \quad (1)$$

In the aforementioned equation, \bar{f}_i is representative of the thrust force added to the flow in the i direction by the presence of the wind turbines. Typically, this force is in the streamwise direction only; thus, in equation, the subscript corresponds only to x .

In this formulation of the boundary layer equation and all subsequent equations, the engineering convention is used so that u , v and w correspond to the streamwise (x), wall-normal (y) and spanwise (z) velocity components, respectively, rather than the atmospheric sciences convention, where z is typically the vertical direction. In all equations in this section, a capital letter indicates an ensemble mean value and a lower case letter indicates a turbulent fluctuation from the mean values according to the Reynolds decomposition. The overbar represents time average.

Multiplying equation (1) by the mean streamwise velocity U_i and rearranging yields the mean mechanical energy equation in which the mean kinetic energy in the flow is described by the sum of $\frac{1}{2}U_i^2$ as,

$$U_j \frac{\partial \frac{1}{2}U_i^2}{\partial x_j} = -\frac{1}{\rho} U_i \frac{\partial P}{\partial x_i} + \overline{u_i u_j} \frac{\partial U_i}{\partial x_j} - \frac{\partial \overline{u_i u_j} U_i}{\partial x_j} - \mathcal{F}_x. \quad (2)$$

The left-hand side of equation (2) is composed of the convection of the mean kinetic energy in the flow. The terms on the right-hand side of the equation are associated with power added to the flow by a mean pressure gradient, the production of turbulence kinetic energy, the derivative of the flux of turbulence kinetic energy and power extracted by the wind turbine, respectively. Although this equation holds true theoretically for the mean kinetic energy in a wind turbine array boundary layer, further simplifications can be made on the basis of a closer look at the wakes analyzed in the succeeding sections. The turbulence terms of equation (2) are explored in the results of the current work.

To verify the energy balance suggested by equation (2), quantities such as the flux of turbulence kinetic energy and turbulence production need to be quantified within the flow. As aforementioned, the dissipation of energy by turbulence should be of negligible order of magnitude. The flux of turbulence kinetic energy is generally denoted as

$$F_{ij} = -\overline{u_i u_j} U_i. \quad (3)$$

F_{ij} is also an indicator of the degree to which kinetic energy from outside the wake is entrained into the flow. As energy is transported from above the turbine canopy into the wake layer, the wakes themselves are dissipated and the boundary layer recovers toward inflow conditions.

The turbulence production tensor is generally written as,

$$\mathcal{P}_{ij} = -\overline{u_i u_j} \frac{\partial U_i}{\partial x_j}, \quad (4)$$

and quantifies how much of the mean flow kinetic energy has been converted into turbulence. From the perspective of successive wind turbines in an array, the turbulence production, \mathcal{P}_{ij} , represents the amount of energy extracted from the mean boundary layer and no longer available for power production by the device. Energy is furthermore resupplied to the flow from above the wind turbine canopy through the flux of kinetic energy, F_{ij} .

The power produced by wind turbines operating in the ABL is a function of both the aerodynamic design of the rotor blades and the inflow to the turbine. The power output of the wind turbines can be measured in either of two senses (see the work by Kang and Meneveau¹⁷ for more detail), as electrical power,

$$P_{\text{elec}} = \frac{V_{\text{out}}^2}{R}, \quad (5)$$

in which V_{out} is the output voltage of the generator forming the nacelle of the wind turbine and R is the effective resistance of the circuit containing the generator, or as mechanical power,

$$P_{\text{mech}} = T_{\text{wt}} \omega, \quad (6)$$

in which T_{wt} is the mechanical torque of the turbine rotor and ω is the angular momentum of the rotor.

As generators are mechanical devices subject to losses of energy, several factors act to significantly decrease the generator efficiency.^{17,18} These factors include losses in the copper coils via the dissipation of heat in the windings of the generator, magnetic losses in the induction processes converting magnetic fields to electrical current, and mechanical losses from friction between the bearings suspending rotating parts and the bushings or brushes of the generators. Also included in friction-type losses is the air-friction loss of the rotating armature forming the wind turbine rotor. Because of losses of these types, the measured values of P_{elec} are expected to be significantly lower than directly measured values of P_{mech} .

The net power *available* to the wind turbine is commonly defined as,

$$P_{\text{fluid}} = \frac{1}{2} \rho U_{\text{eff}}^3 A, \quad (7)$$

where ρ is the density of the air, considered here to be constant, and $U_{\text{eff}} = \frac{1}{A} \int U dA$ is the effective mean velocity across the rotor area upstream of a particular turbine and the rotor disc area, $A = \pi D^2/4$. P_{fluid} is derived directly from the conservation of momentum along streamlines in Bernoulli's principle.

The power coefficient of a wind turbine can be computed directly with the aforementioned equations as,

$$c_p = \frac{P_{\text{mech}}}{P_{\text{fluid}}} = \frac{T_{\text{wt}} \omega}{\frac{1}{2} \rho U_{\text{eff}}^3 A}. \quad (8)$$

Typically, the mechanical power, P_{mech} , is used as the wind turbine power, P_{wt} , as it is expected to scale much better between wind tunnel experiments and real turbine installations being free from the difficulty to diagnose losses detailed above. Thus, with measurements of mechanical torque T_{wt} and angular velocity, ω , the power coefficient can be calculated when coupled with flow velocity measurements.

The tip speed ratio of wind turbines is a characteristic number with which experiments are commonly scaled and performance of turbines is gauged.¹ The tip speed ratio is commonly defined as,

$$\lambda_{\text{tsr}} = \frac{\frac{D}{2}\omega}{U_{\text{eff}}}, \quad (9)$$

and is a ratio of tangential velocity of the tips of the rotor blades to the mean streamwise velocity across the rotor area. Typical values of tip speed ratios range from $4 < \lambda_{\text{tsr}} < 5.5$, with optimal ranges of up to $\lambda_{\text{tsr}} = 7$ depending on rotor blade design and particular flow character.¹⁹

3. EXPERIMENTAL DESIGN

3.1. Wind tunnel facility

The facility at Portland State University consists of a closed-circuit wind tunnel with a contraction ratio of 9:1 to ensure low turbulence intensities without set obstructions. The test section has a length of 5 m and a cross section of 0.8×1.2 m. The freestream wind speed may be adjusted in a reliable working range of $2\text{--}40$ m s⁻¹. The test section is comprised of a variable-profile articulated ceiling, fixed non-operators' side wall, floor and operator's-side wall consisting of access panels. This ensures easy access to the tunnel and the capability of imposing positive or negative streamwise pressure gradients. The test section cross-sectional area gradient is adjustable in the range of $0.55 \text{ m} > dA/dx > -0.55 \text{ m}$, with the distance between the test section floor and ceiling able to be modified between 0 and 0.8 m. For this experiment, the ceiling was maintained parallel to the test section floor. A rigid steel framework is designed to serve as the supporting structure for the test section components, and a precision platform for the setup and operation of experiments. All surfaces are constructed of schlieren-grade annealed float glass affixed to the steel framework to ensure maximum access to the non-intrusive laser-based measurement techniques.

Figure 1 shows the experimental setup from the user's side of the wind tunnel. Shown are two out of the four measurement locations obtained via stereographic particle image velocimetry (SPIV). The same relative positioning of SPIV windows were made around the exit row of wind turbines. The wind tunnel was furnished with a passive grid at the entrance of the test section to introduce turbulence. The grid consists of seven horizontal and six vertical rods thus increasing the turbulence intensity and placed far enough upstream of the wind turbine models.

Vertical stakes were fabricated to further modify the inflow of the wind tunnel. The use of vertical stakes has been common practice in wind tunnel experiments in simulating the ABL. The specific shapes and profiles used have varied with application but has been fairly well diagnosed.^{20–22} These stakes are composed of 0.0125 m thick plexiglass and shaped to precondition the boundary layer in the wind tunnel to more closely match observed trends in the ABL. There were nine vertical stakes spaced 0.136 m apart across the width of the tunnel. The stakes were placed 0.5 m downstream of the passive grid.

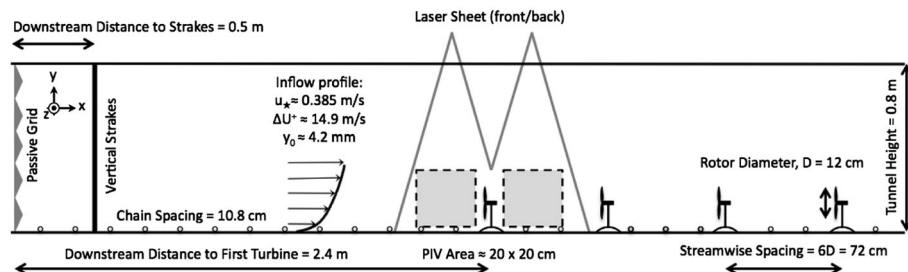


Figure 1. Schematic of experimental setup viewed from the user-side of the wind tunnel. The effective friction velocity, u_* , velocity deficit, ΔU^+ , and effective surface roughness height, y_0 , are included to characterize the inflow. The schematic above is for reference only, dimensions are not to scale.

As a final conditioning element for the inflow of the experiment, semi-porous surface roughness was added to the floor of the wind tunnel via small-diameter chains. The chains have an average diameter of approximately 0.0075 m. The introduction of surface roughness to the boundary layer extends the influence of the high shear zone.

Wind turbines operate in the ABL rather than standard flat plate boundary layers, where the law of the wall is properly applied. This places the experiment in conditions similar to other wind tunnel experiments.¹³ The boundary layer is characterized with three parameters: an effective roughness scale, the friction velocity and a boundary layer velocity deficit. The friction velocity, u_τ , and wall friction, τ_w are defined as,

$$u_\tau = \sqrt{\frac{\tau_w}{\rho}} \quad \text{with} \quad \tau_w = \mu \frac{\partial U}{\partial y} \Big|_{y=0}. \quad (10)$$

However, as is often the case in wind turbine studies in wind tunnel SPIV experiments, measurements are not made sufficiently close to the ground to resolve the gradient at the wall. Instead, the friction velocity is evaluated as $u_* = \sqrt{-\bar{u}\bar{v}}$ in the constant shear layer, where $\partial(-\bar{u}\bar{v})/\partial y = 0$. The subscript change from τ to $*$ indicates that this is an effective value of the friction velocity rather than that according to the classical definition. Defining a velocity shift, ΔU^+ , and effective surface roughness, y_0 , one can use the relationship,

$$\Delta U^+ = B + \frac{1}{\kappa} \ln \left(\frac{u_* y_0}{v} \right), \quad (11)$$

in the log layer of the boundary layer. In equation (11), the constant $B = 5.5$ and the von Kármán constant is taken as $\kappa \approx 0.4$. With these parameters, an equation for velocity profile, $\tilde{u}(y)$, is given as:

$$\tilde{u}(y) = u_* \left(\frac{1}{\kappa} \ln \left(\frac{u_* y}{v} \right) + B - \Delta U^+ \right). \quad (12)$$

Equation (12) is the mean streamwise velocity profile upstream of the wind farm. Parameters for the data fit indicate that the boundary layer in the wind tunnel matches those of the ABL in ‘open field’ conditions²³ as well as other wind tunnel experiments containing model wind turbines.^{10,11,15,24} The effective friction velocity obtained from the fit of the velocity profile in the log layer was $u_* = 0.385 \text{ m s}^{-1}$. An alternate means of estimating the friction velocity was used to verify this value. Calculating $u_* = \sqrt{-\bar{u}\bar{v}}$ in the constant shear layer yielded a value of $u_* = 0.32 \text{ m s}^{-1}$. The comparison of these two methods serves to demonstrate that the inflow is well conditioned as shown in Figure 2.

Further characterization of the approach flow to the wind turbine array model used in the experiment are detailed by Figure 3. Spatial coordinates were normalized according to the turbine rotor diameter, D . Mean velocity profiles (Figure 3(a)) show that the current turbine rotors are well within the modelled boundary layer at $y/D = 0.5$ to $y/D = 1.5$, as previous wind tunnel experiments for wind turbines.^{13,24}

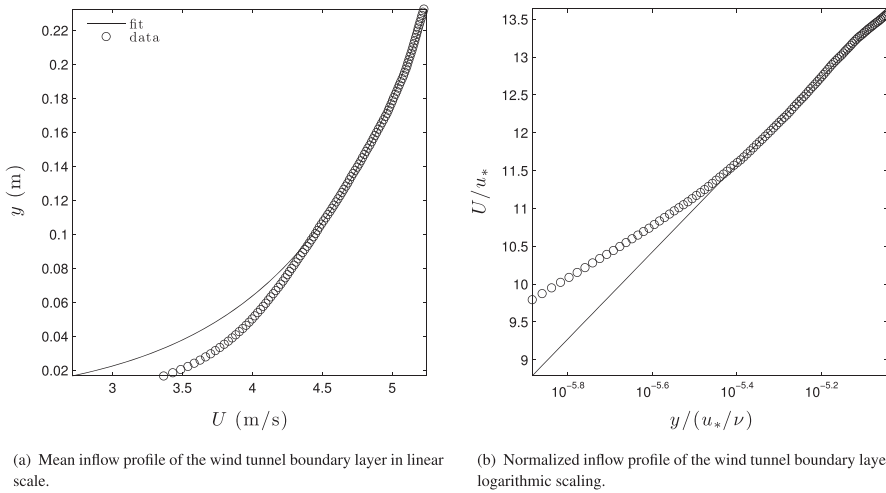


Figure 2. For the inflow, a fit line was generated according to equation (10) in the log layer (specifically, y varies from 0.108 to 0.233 m). The effective friction velocity, u_* , was calculated to be 0.385 m s^{-1} and the effective roughness 10^{-4} m . This leads to a velocity deficit of $\Delta U^+ = 14.9 \text{ m s}^{-1}$.

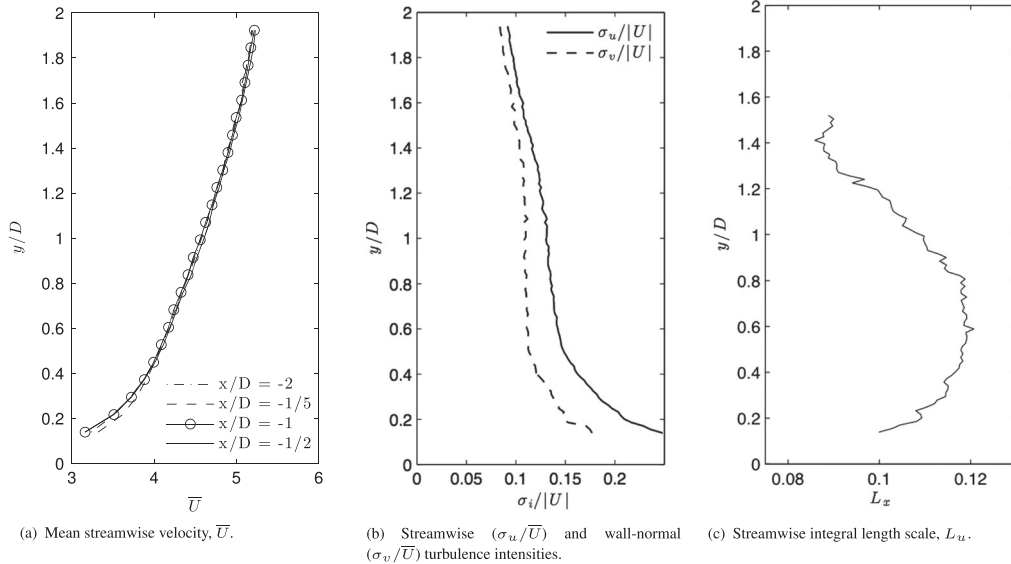


Figure 3. Characteristic quantities of the wind tunnel boundary layer in the approach flow upstream of the wind turbine array. Spatial coordinates, x and y , have been normalized by the wind turbine rotor diameter.

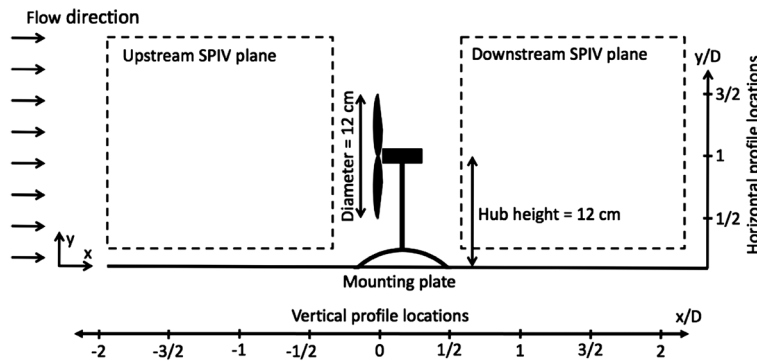


Figure 4. Side view of wind turbine model showing the relative location of SPIV planes and profile locations. The normalized wall-normal coordinate, y/D begins at the floor of the wind tunnel, and the normalized streamwise coordinate begins at the turbine rotor.

Turbulence intensities (Figure 3(b)) show peak values near the wall as expected for a boundary layer. In the range of the turbine rotor, the turbulence intensity is slightly greater than that of other research because of the presence of the passive grid and vertical strakes. These conditioning elements are absent from other experiments. The increased turbulence intensity in the inflow is desirable as the primary goal is characterizing wind turbine wakes in terms of the production and flux of turbulence kinetic energy. The streamwise turbulence ranges from 12 to 15% in the region of the turbine rotor. The integral length scale (Figure 3(c)) in the rotor area of the approach flow is of the same order of magnitude as the rotor diameter, which is important in generating large-scale effects in the wind turbine array as reported in the studies by Espa  a *et al.*^{25,26}

3.2. Instrumentation

The SPIV data in this experiment were collected in two windows simultaneously as shown in Figure 4, which is for windows directly upstream and directly downstream of the centerline entrance-row and exit-row turbines in the array. The SPIV consisted of LaVision system with an Nd : Yag (532 nm, 1200 mJ, 4 ns duration) double-pulsed laser and four

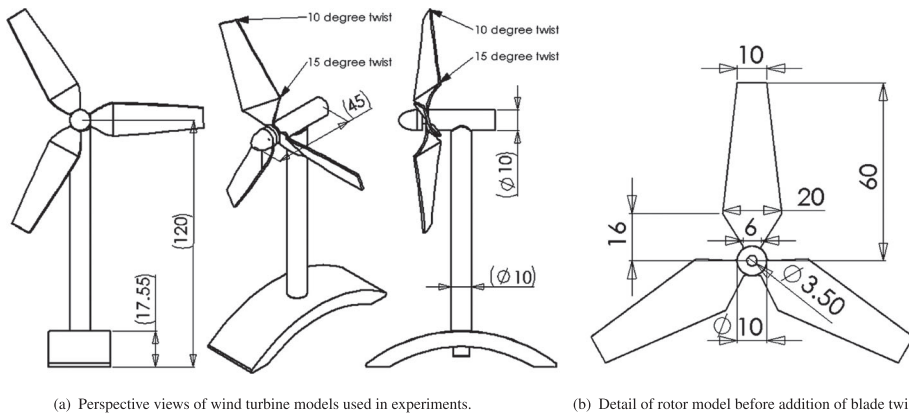


Figure 5. Technical drawing of model wind turbines used in experiments. The rotor blades were designed such that the widest part was pitched to 15° from the plane of the hub. The tips of each blade were pitched to 10° from the plane of the hub. All dimensions are in millimeters. Note that the mounting plate shown in Figure 5(a) spans the full width of the wind tunnel and only a small section is shown.

4MP ImagerProX charge-coupled device (LaVision GmbH Anna-Vandenhoeck-Ring 19 D-37081, Goettingen, Germany) cameras arranged in pairs for the two SPIV windows. The flow was seeded with neutrally buoyant fluid particles of diethylhexyl sebacate and allowed to mix thoroughly. Seeding was kept at a constant level throughout experimentation to ensure consistent seeding density within the measurement place. The laser sheet was approximately 0.001 m thick with a divergence angle of less than 5 mrad across the span of measurement locations shown in Figures 1 and 4. A single laser sheet was used for both measurement locations and was blocked in the center to reduce reflections from the turbine assemblies.

The cameras were calibrated before each measurement set using a standard two-plane measurement plate with specific geometries recognized by the measurement software. The resulting measurement windows were approximately $0.23 \text{ m} \times 0.23 \text{ m}$ with a vector resolution of approximately 1.5 mm. The uncertainty of each measurement was within approximately 3% with the greatest uncertainty pertaining to the out-of-plane (spanwise) component, although the error is difficult to estimate in this direction. For this reason, spanwise velocity data is omitted from the following results.

At each measurement location, 2000 SPIV image sets were collected. Raw images were processed into vector fields using a multipass Fast Fourier transform-based correlation algorithm of reducing size interrogation windows (twice at 64×64 and once at 32×32 pixels) with a 50% overlap. With a delay between image pairs of $130 \mu\text{s}$, an average particle displacement of eight pixels was obtained. Erroneous vectors were on the order of 1% of the total calculated vectors and were replaced with a Gaussian interpolation of valid neighboring vectors.

3.2.1. Wind turbine models

The turbine models were fabricated in-house according to a design specified to simulate dynamics observed in full-scale turbine arrays. The rotor blades were laser cut from 0.0005 m thick steel sheet and formed to shape using a positive/negative die press to ensure uniformity. The die press was designed in-house using three-dimensional CAD software (Dassault Systèmes SolidWorks Corporation, 175 Wyman Street, Waltham, MA 02451, USA) and set each of the rotor blades to a pitch of 15° from the plane of the rotor and a 10° twist at the tip illustrated by Figure 5.

The nacelle of each turbine consisted of an electric motor (Faulhaber GMBH & Co Series 1331T012SR) acting as a generator mounted to a 0.01 m hollow steel shaft. The motors were cylindrical with an outside diameter of 0.013 m and a nominal operating voltage of 12 V and a no-load current of 0.0105 A. The motors were aligned with the flow with the shaft pointed upstream. The mast was cylindrical in geometry and the hollow interior allowed for electrical wiring for the motor/generator and the torque system (detailed in the succeeding text) to be removed from the flow. Figure 5 shows schematics of the fully assembled turbine models including mast, nacelle, rotor, mounting plate and a detail view of the rotor before blade twisting. Power measurements were made with the torque sensing device outlined in the succeeding text. When collecting velocity data, the torque sensor was removed so that the turbine models were as shown in Figure 5.

3.2.2. Torque sensing system

The torque sensing system implemented in the experiment here followed the design and procedure outlined in the work by Kang and Meneveau¹⁷ in which a housing was built to hold the electric motor described in the previous text such that it was free to rotate along its operating axis. The motor acting as a generator was supported in a solid metal housing by two identical VXB (NationSkander California Corp., 2165 S Dupont Dr Ste F, Anaheim, CA 92806, USA) ball bearings aligned concentrically with the shaft of the generator. The inner and outer diameters of the bearings were 0.013 and 0.024 m

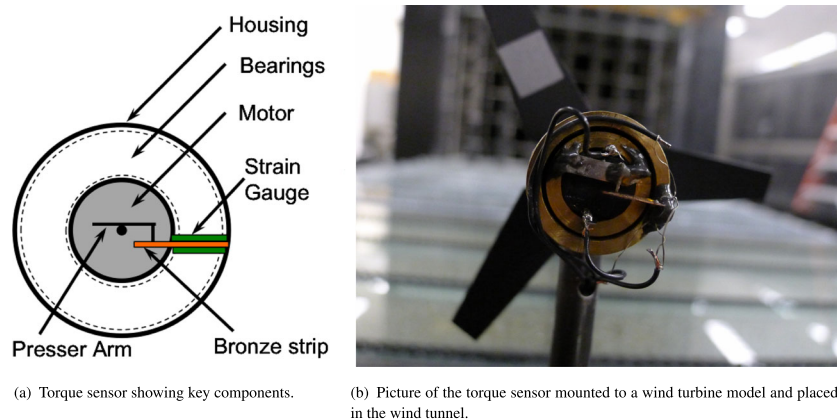


Figure 6. Schematic (a) and picture (b) of the torque sensor used in the experiment. The reflective tape shown in the top rotor blade in (b) was used in the optical measurements of angular velocity.

respectively, and the outer diameter of the housing was approximately 0.0254 m. The bearings allowed the entire generator to freely rotate in reaction to the application of torque to its shaft. On the downstream side of the motor/bearing housing, a pressing arm with a pin was attached such that any applied torque resulted in the flexure of a sensitive bending plate consisting of a 0.0025 m wide strip of 0.0005 m thick bronze, 0.02 m in length. Mounted to the bronze strip were two small 120Ω linear strain gauges (OMEGA SGD-3/120-LY11) that measured the torque required to keep the motor at the same relative alignment in the tunnel. Figure 6 shows the assembly of the motor/bearing housing labeling the important components.

The two strain signals from the flexure of the bending arm were measured with a Wheatstone bridge constructed with four 120Ω linear strain gages. The two resistors not fixed to the flexure arm required to form a complete bridge came from strain gauges of identical type mounted to a 0.1 m aluminum cube. The entire strain-gauge/bridge system was conditioned and amplified by an external electrical module (OMEGA DMD-465 Bridgesensor) and measured at 10 kHz via LabVIEW and a National Instruments DAQ (National Instruments Corporation, 11500 N Mopac Expwy, Austin, TX 78759-3504, USA).

Tip speeds were monitored through a Monarch optical tracker with a working range of 1 – 250000 rpm. Rotational speeds were controlled by applying resistive electrical loads to the motors. Each row of turbine models was set to operate under loading conditions corresponding to the peaks of their power curves, discussed in Section 4.1. The masts were hollow allowing electrical wiring for speed control and other measurements to be contained and out of the mean flow mitigating added effects in the main wake area.

To ensure accurate measurements of torque and power, the strain gauges used in the torque sensors were calibrated before collection of data in each measurement location. Calibration of strain gauges was executed according to manufacturer specifications by applying a static load between 0.2 and 5.5 g to the bronze armature fixed to the sensor. These calibration curves were used to correct data from the dynamic loading of the strain gauges acquired in experiments.

Measurements were made of the resistive load of the circuits containing the turbine models and their rates of rotation in order to calculate wind turbine power according to equation (6). The loading in the experiment was tuned to the design specifications of the electric motors comprising the nacelles of the turbine models. Loads varied from $2\ \Omega$ to $10\ k\Omega$.

3.3. Test cases

Several configurations of the wind turbine array were tested in the wind tunnel. The data here correspond to a comparison of the base case (a four by three Cartesian arrangement) and two iterations of a row-offset arrangements. Streamwise spacing of rows and spanwise spacing of turbines (within each row) was fixed for all configurations at 6 rotor diameters in the streamwise direction and 3 rotor diameters in the spanwise direction and denoted S_x and S_z , respectively. An overhead view of each configuration can be seen in Figure 7. In the figure and throughout the paper, the test cases are referred to with abbreviated titles. For the base arrangement, the entrance row turbine is base-center-front (BCF), and the exit row is base-center-back (BCB). For the row-offset arrangements, the entrance row is offset-center-front (OCF) and the exit row turbines are offset-center-1back (OC1) and offset-center-2back (OC2), respectively, for the first and second variations.

The intended investigation makes use of the change of wind turbine spacing in a streamwise sense. In the row-offset cases, the spacing between turbines along the x -coordinate is effectively doubled while maintaining a similar turbine density within the array. The doubling of streamwise turbine spacing allows a significant increase in the remediation of

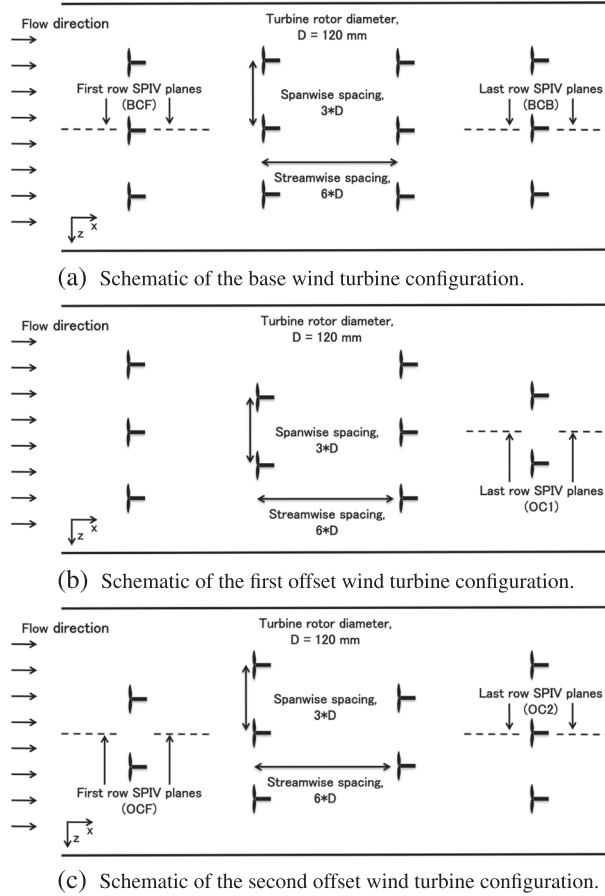


Figure 7. Schematic of the wind turbine array configurations for the wind tunnel experiments. In all cases, the streamwise spacing between rows is six times the rotor diameter (0.72 m). The spanwise spacing between turbines is three rotor diameters (0.36 m). S_x and S_z refer to the streamwise and spanwise wind turbine spacing, respectively.

wakes before the inlet of successive turbines.^{13,16} The change in arrangement also increases spanwise entrainment of high-momentum flow into the wake areas although this particular behavior is not the focus of the current research.

The row-offset cases shown in Figure 7 address the issues of perceived underperformance of wind turbines placed in the wakes of preceding devices. The work by Saranyasoontorn and Manuel²⁷ shows the effects of turbulence as fatigue loading on a wind turbine blade. Similar studies have been carried out as in the work by Frandsen and Thogersen,²⁸ where the combined effects of ambient turbulence and wind turbine wakes were discussed from the perspective of loading. Similar wind turbine array schemes were used in the experiments by Chamorro *et al.*,^{13,14} where the spacing between wind turbines was slightly reduced as compared with the present experiment and the model wind farm had additional rows.

4. RESULTS

4.1. Power production

The power produced by the wind turbine models is increased in the offset cases over that of the base case because of the effective increase of downstream turbine spacing from 6 rotor diameters to 12 as shown in Figure 7. In both variations of the offset arrangement, the second row turbines produced approximately 90% of the power measured for the entrance row. These results are expected, as there are no direct upstream obstructions, and they receive a nearly undisturbed inflow.

Curves of the power coefficient, c_p , according to tip speed ratio, λ_{tsr} , are shown in Figure 8. According to the figure, the offset case outperformed the base arrangement for both the entrance and exit rows wind turbine models. The entrance row of both arrangements show the peak value of c_p occurring at $\lambda_{tsr} \approx 3$. The peak of the exit row of the offset case shows a peak value closer to $\lambda_{tsr} = 3.5$. Velocity measurements used in calculating U_{eff} are local values calculated from

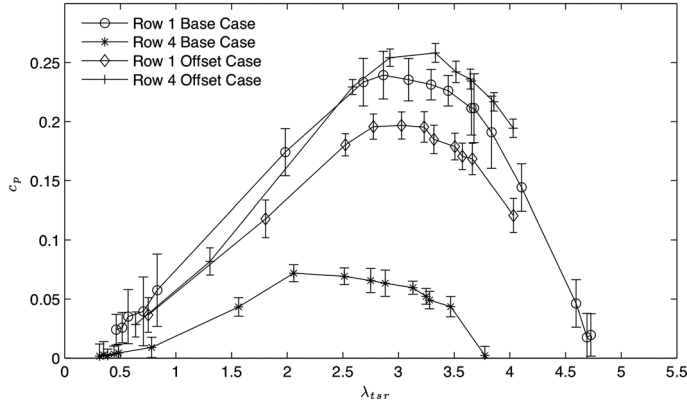


Figure 8. Curves of power coefficient c_p by tip speed ratio λ_{tsr} according to equations (8) and (9), respectively. The exit row turbine performance shows a fivefold improvement from the base arrangement to the offset arrangement. The velocity, U_{eff} , used in calculating c_p is a local effective velocity for each wind turbine. Error bars in figure correspond to the variance of the recorded signals.

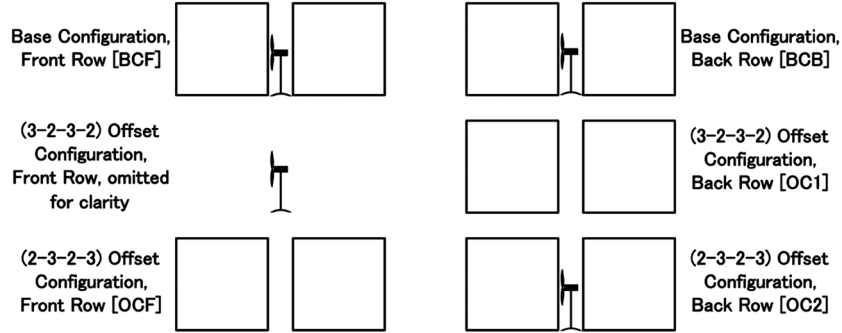


Figure 9. Measurement locations displayed in the following contour plots. Note that the data for the front row of the (3 – 2 – 3 – 2) offset configuration (center row) have been omitted as they are statistically identical to those of front row of the base configuration. The three measurement locations immediately upstream and downstream of wind turbines are marked with a turbine in the figure.

Those without the turbine (OC1 and OCF) are empty positions within the offset arrays.

measurements directly upstream of each wind turbine. The power coefficients and tip-speed ratios seen in the figure are lower than would be expected for devices in the field but are at a reasonable level for wind tunnel experiments. The variance of the measured c_p values for the case BCF had a maximum value of 0.031 or 4.1% compared with the mean, at $\lambda_{tsr} \approx 3.75$. For other measurement cases and tip-speed ratios, the variance was on the order of 1.5–2.0%. Variance of the power signals is shown in the curves of c_p in Figure 8.

In this experiment, the rotor blades are not airfoils but shaped sheet metal. The rotors at the given Reynolds number experience high drag, contributing to the relatively low power coefficient compared with full-scale devices.

4.2. Mean flow results

Many of the figures presented display data in three formats described in the succeeding text. Note that data pertaining to the entrance row of the (3 – 2 – 3 – 2) offset case has been omitted from the current results as they are statistically identical to the entrance row of the base arrangement. The locations of data in contour plots are shown in Figure 9 including acronyms for each measurement case in square brackets. Many of the figures in this chapter conform to one of the following three forms, outlined here for reference:

- **Horizontal profiles:** profiles of the quantity in question are drawn at selected wall-normal locations. Specifically, profiles are drawn at the bottom tip of the rotor, at the turbine hub height and the top tip of the rotor. In normalized

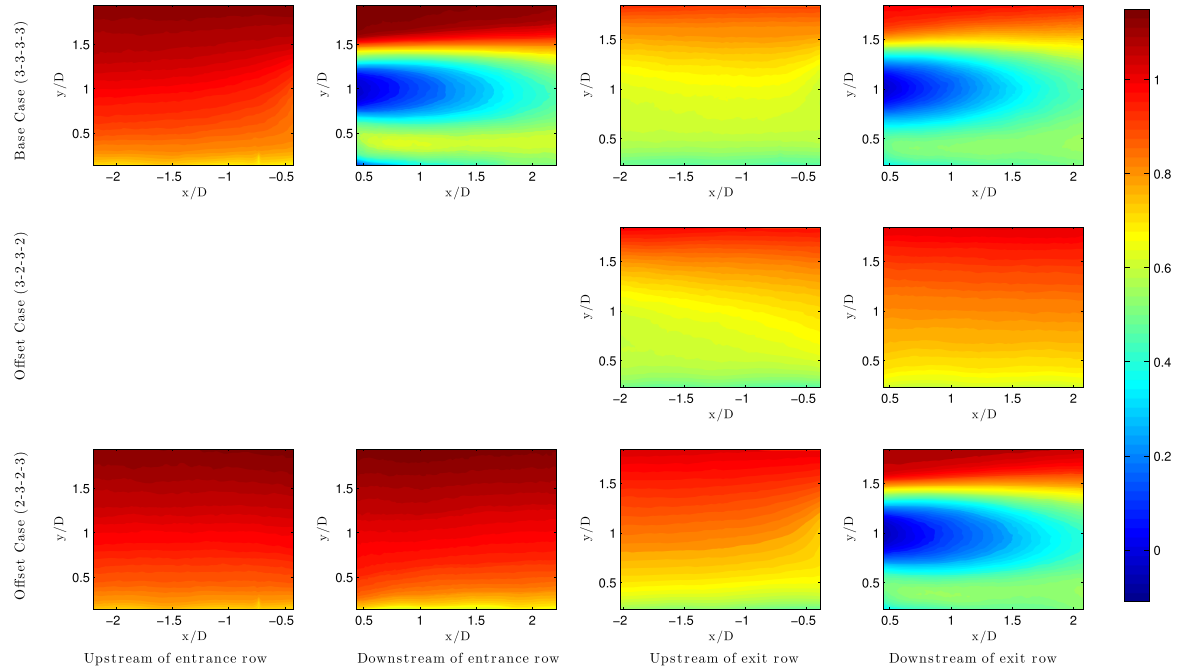


Figure 10. Contours of the normalized mean velocity in the streamwise direction, U/U_{hub} .

coordinates, these locations are $y/D = [\frac{1}{2}, 1, \frac{3}{2}]$. The left pair of subplots correspond to entrance row measurement locations, and the right pair corresponds to the exit row locations.

- **Vertical profiles:** profiles of the quantity in question are calculated in the wall-normal direction at specific values of x/D with respect to the specific turbine location. Specifically, $x/D = [-2, -\frac{3}{2}, -1, -\frac{1}{2}, \frac{1}{2}, 1, \frac{3}{2}, 2]$.
- **Contour plots:** the quantity in question shown for each SPIV plane. Figure 9 shows the positions and names of each SPIV window in the contour planes. The blank spaces in Figure 9 correspond to the entrance row of the first offset configuration. Because these positions are statistically identical to BCF, they have been omitted from the analysis.

In the following profiles and contours, the mean velocity was normalized with the mean streamwise velocity at the hub height of the wind turbines according to U/U_{hub} . The Reynolds stresses were normalized with the square of the hub velocity as $-\bar{uv}/U_{hub}^2$. In all cases, the hub height velocity, $U_{hub} = 4.6 \text{ m-s}^{-1}$ was used for normalization of velocities and stresses. The Reynolds number of the entrance row turbines based on the hub height velocity and rotor diameter is approximately 3.7×10^4 . At this level, the Reynolds number is on the same order of magnitude of the Reynolds number independent range detailed in the work by Chamorro *et al.*²⁹ The production of turbulence and the flux of kinetic energy have not been normalized.

The following sections detail the characterization of the wind turbine wake flow from the current experiment. Section 4.2 describes the mean flow field in the locations described in the previous text. Reynolds normal and shear stresses are presented in Section 4.3. Results pertaining to the turbulence production, P_{ij} , and the flux of kinetic energy, F_{ij} , are discussed in Section 4.4.

By design of the experiments, the SPIV window upstream of the front row turbines should be statistically identical for all configurations of the array except in the region very near ($x/D > -1$) a turbine model. In OCF, where there is no turbine, the upstream SPIV plane shows the development of the undisturbed boundary layer. For this reason, this window is used as a basis for comparison of wake positions and locations within the wind turbine array. The downstream position of OCF, however, includes effects of the mounting plate for the turbines shown in Figure 5(a).

Looking first at the contours of mean streamwise velocity, U/U_{hub} , in Figure 10, one observes the similarity between the inflow fields of BCF and OCF, as expected. In both cases, there are no upstream obstructions other than those used to shape the inflow. In the exit row positions (BCB, OC1, and OC2), the inflow fields are immediately upstream of the exit row of turbines in the array.

Seen in the contours of BCF and OCF, there is a small difference in close proximity ($x/D > -1$) to the turbine hub. In BCF, one can see a reduction in the mean streamwise velocity due to blockage of the flow. This blockage in U results in an acceleration of the flow in the wall-normal and spanwise directions thus one can also observe in Figures 11(b) and 12(b) a

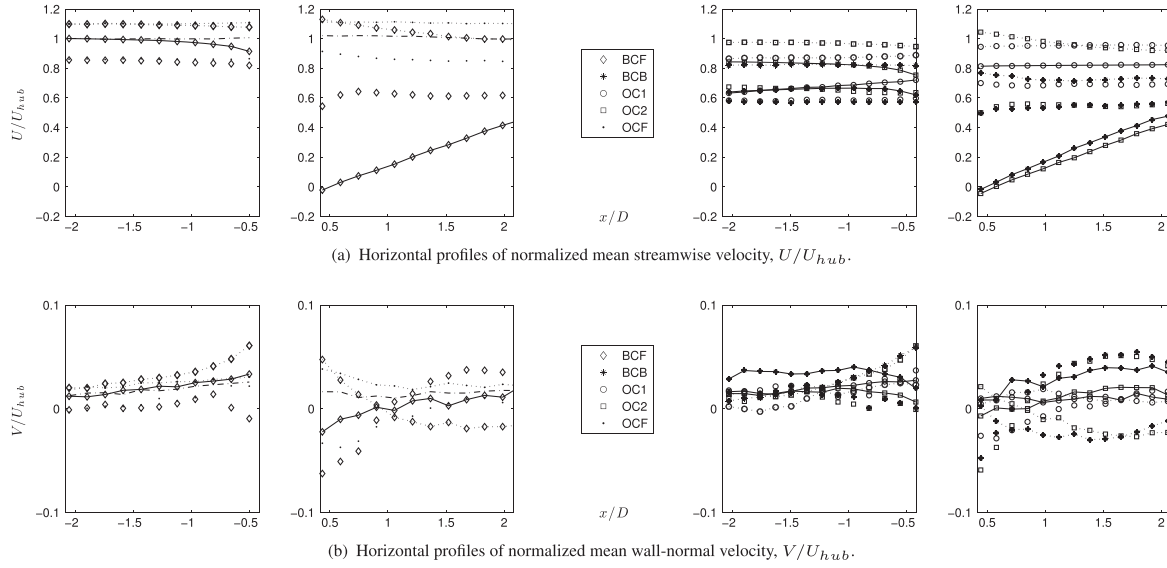


Figure 11. Profiles of mean velocity with the streamwise coordinate. Profiles correspond to the hub height (markers with lines), top rotor tip (markers with dotted lines) and bottom rotor tip (markers without lines). The left pair of figures correspond to the entrance row turbine locations and the right pair to the exit row turbine locations.

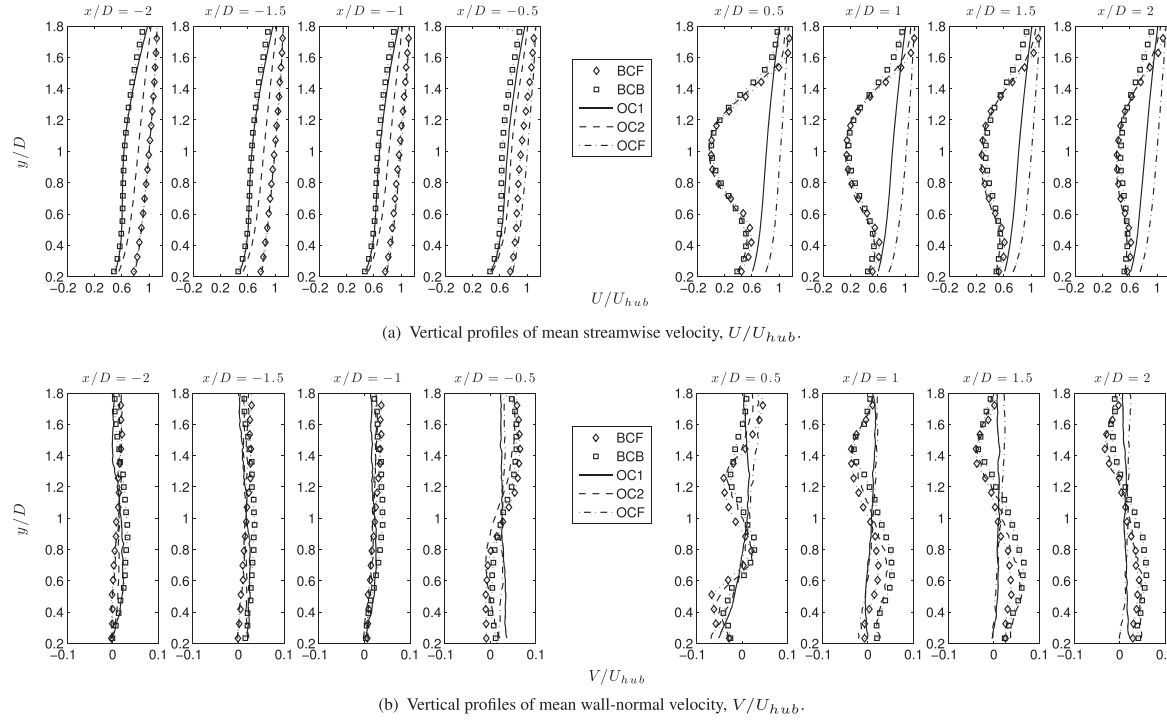


Figure 12. Profiles of mean velocity with the wall-normal coordinate. Profiles are taken at half-diameter increments upstream and downstream of wind turbine model.

spreading of the flow around the turbine for BCF. Recalling that the inflow for OCF is essentially the undisturbed inflow, one observes V/U_{hub} in the range from -0.011 to 0.0325 . In comparison, the extreme values of V/U_{hub} in the upstream section of BCF are on the order of 0.075 near the top tip of the rotor and -0.022 near the bottom tip of the rotor, twice that of OCF.

Looking at the inflow planes for the exit row turbine position (BCB, OC1 and OC2), the same streamwise blockage effect and vertical acceleration is visible wherever a turbine is present. In OC1, there is no turbine, and the field shows

the far-wake ($4 < x/D < 8$) recovery of the third row turbine. In all three of the exit row SPIV planes, the mean profiles of U/U_{hub} are decreased as the wake has not fully recovered. Where a turbine is present, the spreading effect viewed in V/U_{hub} is approximately 15–30% less intense than in the entrance row. This decrease in extrema in V/U_{hub} is clearly visible in both the horizontal profiles (Figure 11(a)) and the vertical profiles (Figure 12(b)).

In Figures 10 and 12(a), one can see the wake areas behind in the SPIV planes downstream of the wind turbines. The three wakes occur in BCF, BCB and OC2. Comparing the size and intensity of the three wakes in Figure 10 and described in the previous text, BCF shows the greatest mean flow deficit in U . The immediate implication of this is that BCF extracts the most energy from the wind. The energy available to each successive row of turbines in the array depends on the recovery of the flow between turbine rows. Thus, we expect to see a smaller range of dynamics in the wakes of BCB and OC2. This is confirmed by power coefficient curves generated for the entrance and exit rows in the different array configurations as seen in Figure 8.

Figures 11(a) and 12(a) reflect the softened gradients of U/U_{hub} as well. Comparing the vertical profiles in the wakes of BCF, BCB and OC2, the three wakes are nearly equal in intensity and that the mean streamwise velocity varies from $U/U_{hub} = 1.2$ (slightly less than that of the freestream) to a strong recirculation region behind the nacelle, where $U/U_{hub} = -0.1$ at $x/D = 0.5$. In the exit row of turbines, one can observe that the wakes reach a extreme recirculation velocity of the same order as entrance row turbines, but the inflow velocity in the exit rows are reduced by 30–40%. Also of note is that the momentum deficit region of the wakes is more neatly contained in the entrance row turbines. The exit row cases BCB and OC2 show a greater total deficit compared with the array inflow than BCF because of the development of the turbine canopy layer.

The blockage effect previously mentioned can be seen in the upstream edge of the SPIV windows containing the wakes (seen especially in the vertical profiles at $x/D = -0.5$). This is rapidly overshadowed with the mixing effect produced by the turbines. The extreme values of the wall-normal velocity, V/U_{hub} , are reached in the area of $x/D = 1.0$. Specifically, the wall-normal velocity in the wake regions of BCF range from $V/U_{hub} = -0.0325$ to $V/U_{hub} = 0.076$. The mean wall normal velocity in exit row turbines differs from that of the entrance row in that the maximum value is increased by approximately 30% and occurs deeper in the wake, at $x/D \approx 1.75$ rather than at $x/D \approx 0.5$ for the entrance row. Minimum values of the wall-normal velocity are similar for all turbine positions.

4.3. Reynolds stress results

Mean turbulence forms are visible in the contour plots and profiles of the Reynolds shear stresses. The most dynamically significant stress is the normalized in-plane shear stress, $-\bar{uv}/U_{hub}^2$, in which behavior related to tip vortices can be seen

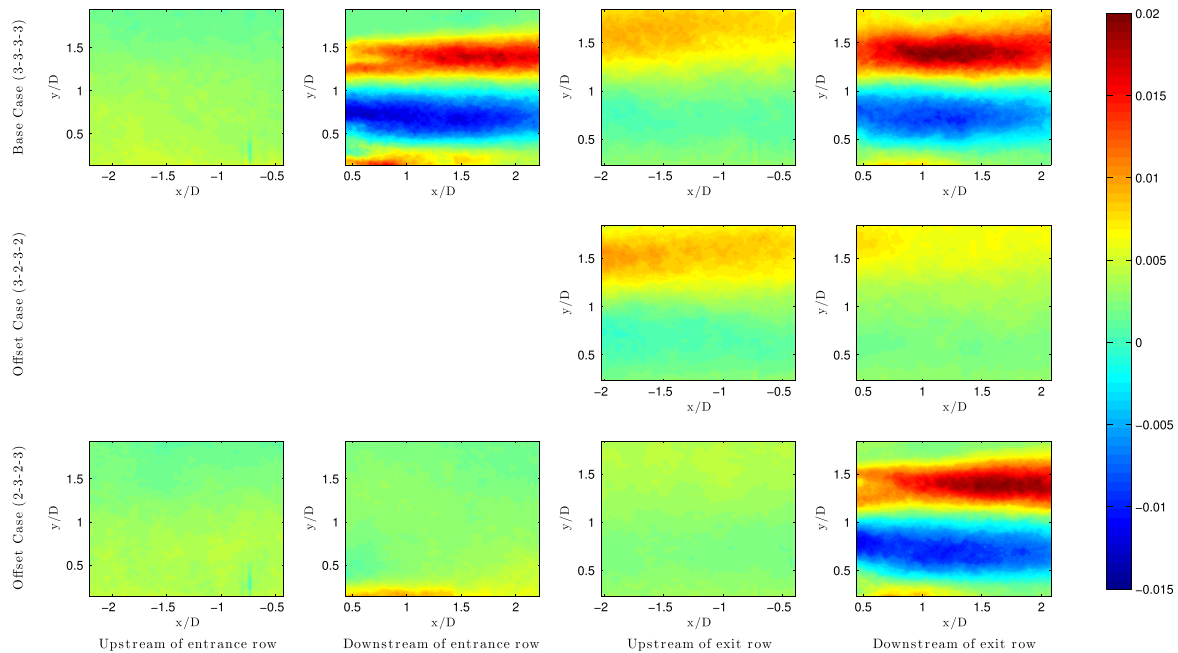


Figure 13. Contour plots of $-\bar{uv}/U_{hub}^2$ for all SPIV locations delineated in Figure 7.

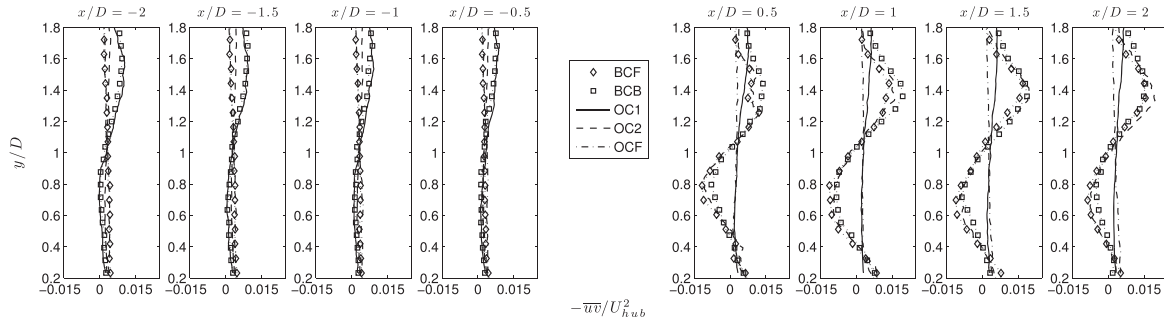


Figure 14. Profiles of the Reynolds shear stress $-\bar{uv}/U_{hub}^2$. Profiles are taken at half-diameter distances upstream and downstream of turbine rows. The maximum values of $-\bar{uv}/U_{hub}^2$ correspond to exit row turbines, whereas the minimum value is associated with the entrance row.

as distinctive regions directly trailing the top rotor tip. Visible in Figure 13, the region of positive $-\bar{uv}/U_{hub}^2$ is always associated with the top of the rotor and has more extreme values than the negatively valued region below the hub. The positive shear stress region also dies off slower than the negative region because of the accentuated gradient of velocity present above the hub height of the model turbines.

A comparison of the inflow measurement locations for exit row turbines shows that the turbulence has only decayed by 50–60% by the subsequent row of turbines. The presence of turbulence in the inflow of the turbine is related to the decrease in power production from the devices as well as the fatigue loading of mechanical components discussed in the work by Saranyasoontorn and Manuel.²⁷

In the wakes of the exit row turbines, we see that the maximum value of $-\bar{uv}/U_{hub}^2$ occurs equally in cases OC2 and BCB. Figure 14 demonstrates that a maximum value is observed on the order of $-\bar{uv}/U_{hub}^2 = 0.022$ in the wakes. The entrance row turbine in BCF reaches a maximum value of $-\bar{uv}/U_{hub}^2 = 0.019$, approximately 14% lower than that of exit row turbines. The minimum value of $-\bar{uv}/U_{hub}^2$, however, occurs in the near wake of the entrance row turbine in BCF and is approximately 15% more extreme than for the exit rows. Chamorro and Porté-Agel^{13,14} have suggested that the turbine canopy is fully developed in the cartesian arrangement of turbines beyond the fourth row. For row-offset arrangements, the fully developed regime in which wakes demonstrate nearly identical dynamics occurs beyond the sixth row.

Results pertaining to stresses including the spanwise component of velocity w have been omitted from the present analysis as their contribution to the turbulent energy budget are less than u and v . Further, the vertical entrainment of kinetic energy from outside the turbine canopy into the wake is most subject to the $-\bar{uv}$ stress and the streamwise velocity U . The turbulence production P_{ij} is also limited in the present analysis to P_{12} for the reason that other components of turbulence production are at least one order of magnitude smaller than that acting in the x - y plane.

4.4. Production and flux of turbulence kinetic energy

The production of turbulence is a quantity that can be used to assess the rate at which energy is removed from the flow available to wind turbines in the array. The contours presented in Figure 15 show clearly that the structures associated with the top and bottom tips of the rotor area are those responsible for the greatest production of turbulence kinetic energy. This also means that the greatest portion of mean kinetic energy converted to turbulence kinetic energy is done by the tip vortices of the rotor blades. Structures arising from the presence of the nacelle and mast in the mean flow contribute orders of magnitude less to the production of turbulence.

Figure 15 highlights the production of turbulence by the passage of the rotor blades in the entrance row of the base arrangement (BCF) and the exit row of the offset arrangement (OC2). The region of the greatest magnitude of production is also well defined in each case and position. This demonstrates that the ‘productive’ region of the wake, in the sense of turbulence, is localized to the near-wake region. In the very near wake, BCB shows a maximum value of production approximately 20% higher than of the other cases, seen in Figure 16. However, as one progresses farther into the wake, maxima are shown equally by the other turbine positions, BCF and OC2.

One of the most important quantities discussed in terms of wake recovery and wind turbines is the flux of kinetic energy, F_{ij} . Recent studies^{15,16} have shown that the entrainment of kinetic energy vertically downward from outside the rotor canopy is a contributor to wake remediation in the turbine array. Figure 17 shows the flux of kinetic energy from measurements taken. As all measurements were taken in the x - y plane, measurement sensitivity was low in the spanwise direction.

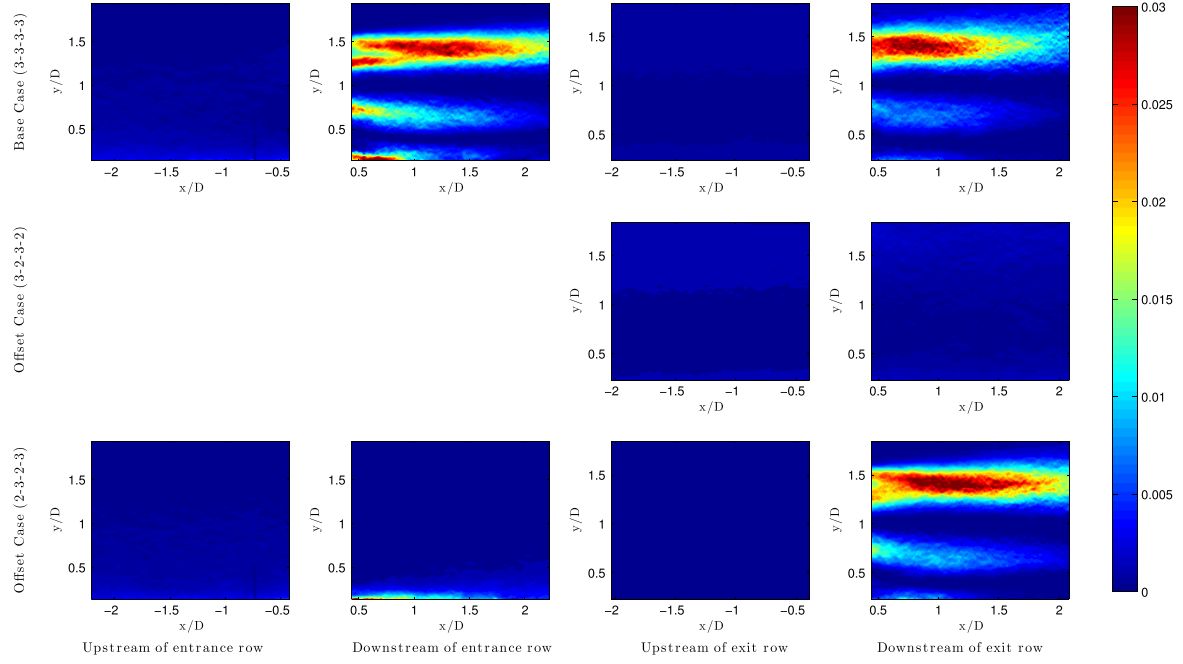


Figure 15. Contour plots of turbulence production. Here, the only component of \mathcal{P}_{ij} shown in $\mathcal{P}_{12} = -\bar{uv}\frac{\partial U}{\partial y}$. The contribution of \mathcal{P}_{12} to the total turbulence production was orders of magnitude greater than other components.

It was also shown that components of F_{ij} involving w or W were orders of magnitude lower than those including only the streamwise and wall-normal components. In Figures 17 and 18, the only component shown is $F_{12} = -\bar{uv}U$ as it is the dominant contributor to the tensor.

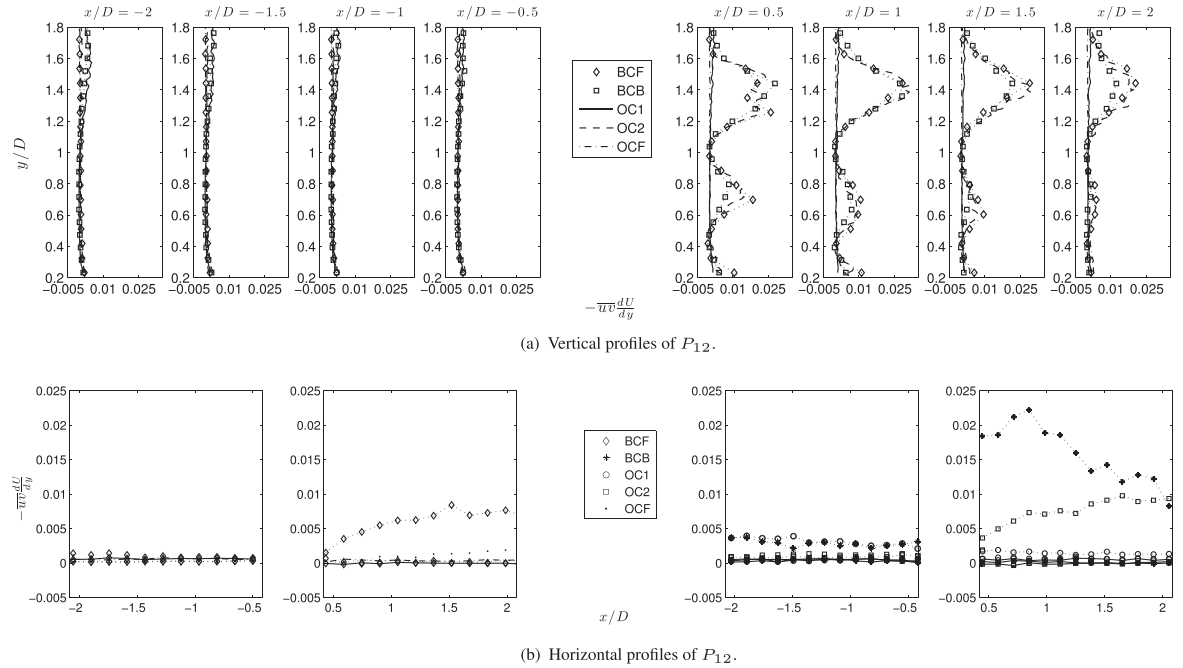


Figure 16. Profiles of turbulence production. Only the in-plane contribution to \mathcal{P}_{ij} is shown. Maximum values in the very near wake area ($x/D = 0.5$) are exhibited by the exit row of the base configuration, BCB. Farther downstream, the maximum value is shown equally by BCF and OC2.

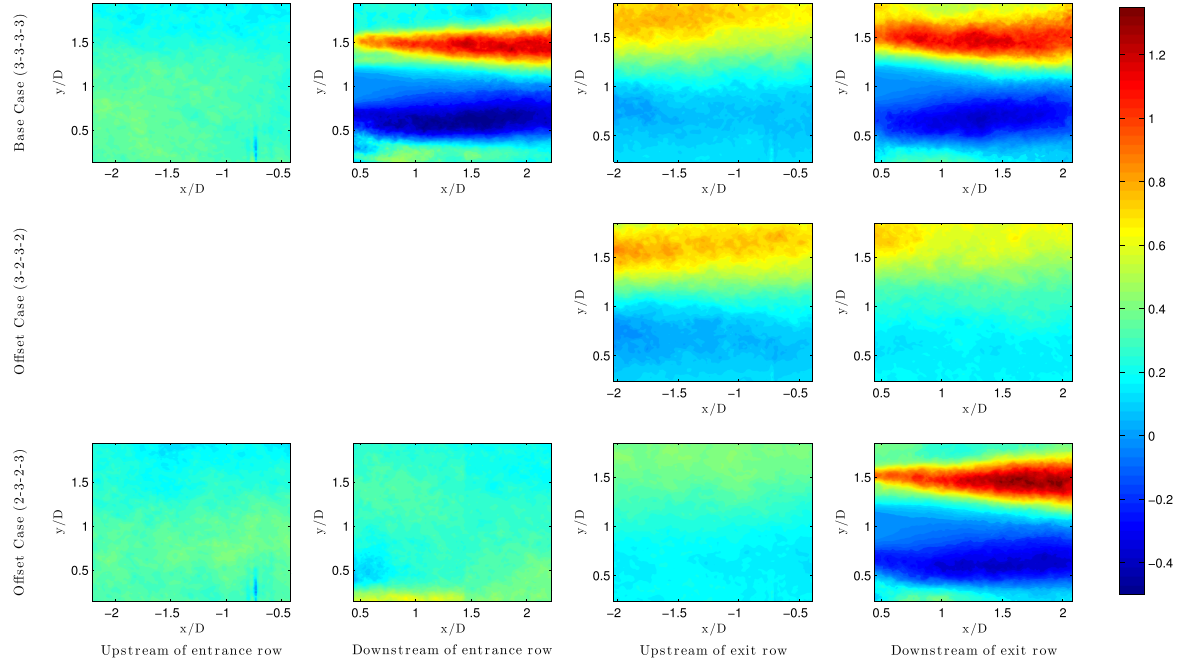


Figure 17. Contour plots of flux of kinetic energy, F_{ij} . As in turbulence production, only the streamwise and wall-normal components are shown as $F_{12} = -\bar{uv}U$ as dominant contributor to the whole.

Note that like in the preceding contour plots, the upstream positions for the entrance rows corresponds to the inflow, free of disturbances. One can observe that in the leftmost subfigures, the magnitude of F_{12} shows a maximum value of about $0.45 \text{ m}^3 \text{s}^{-3}$. In all wake positions, the maximum of F_{12} occurs near the top rotor tip. This is a result of the high level of

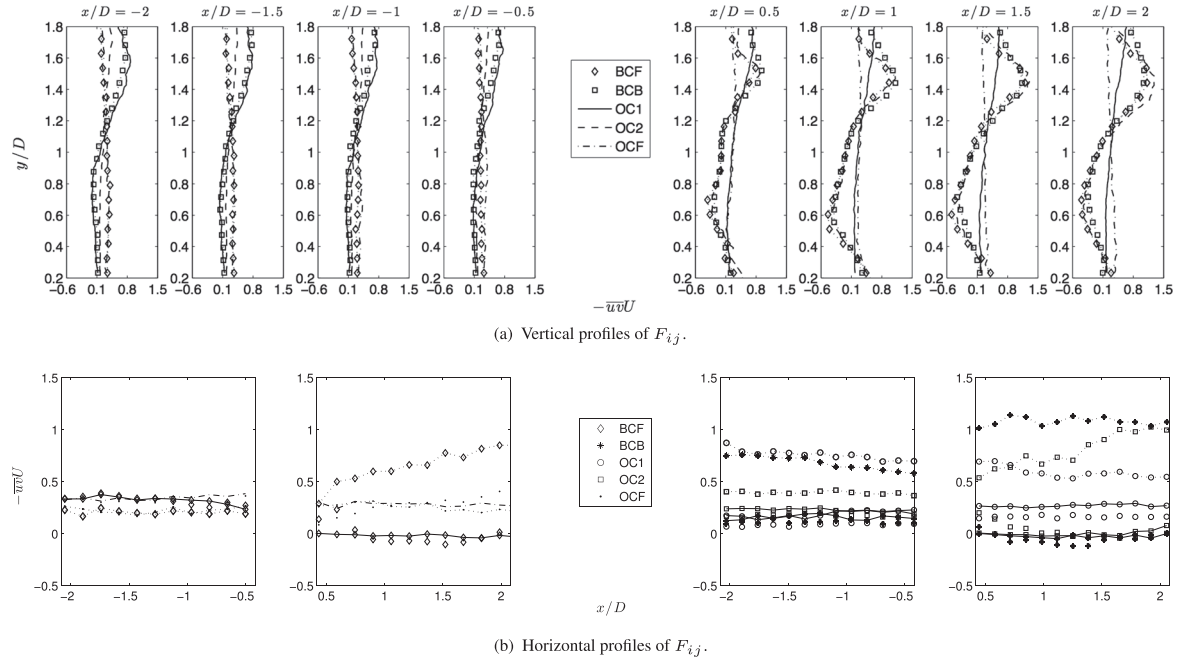


Figure 18. Profiles of the flux of kinetic energy (a). Profiles are taken at half-diameter distances ($x/D = \pm 0.5 \times n, n = [1, 2, 3, 4]$) upstream and downstream of wind turbine model.

agitation in the flow from the combination of a high mean velocity and the periodic presence of a moving solid boundary imparting strong gradients to the flow.

In the right two columns of subfigures (those corresponding to the exit row turbine positions), F_{12} shows a net downward trend even in the far wakes of third row turbines. The bottom row of subfigures shows the (2–3–2–3) offset arrangement in which the wake has had 10 to 12 rotor diameters to recover (bottom right pair). In this position $F_{12} > 0$, implying that 12 rotor diameters downstream of a turbine, the wake is still not recovered, and kinetic energy is still being supplied from above to supplement the momentum deficit in the array.

Turbines that receive an undisturbed inflow or a recovered wake (BCF and OC2, respectively) as inflow demonstrate much more localized regions of positive flux of kinetic energy. In BCF, the maximum value of $F_{12} = 1.3 \text{ m}^3 \text{s}^{-3}$ occurs near $x/D = 1.5$. In contrast, F_{12} in BCB reaches a maximum of approximately $1.2 \text{ m}^3 \text{s}^{-3}$, about 7.5% less than the entrance row, and is more distributed across the top portion of the wake. The reduction and distribution of F_{12} in BCB is an effect of a more fully developed turbine canopy layer. There, the mean flow is reduced and has less momentum to draw into the main wake area. The exit row of the (2–3–2–3) offset case shows a maximum value of $F_{12} = 1.4 \text{ m}^3 \text{s}^{-3}$, approximately 7.5% greater than in the entrance row.

Also seen in Figures 17 and 18 is the region associated with the bottom rotor tip, in which $F_{12} < 0$. In the lower turbine wake, the flux of kinetic energy is *upward* toward the region of greatest momentum deficit. In this area, the extreme value of F_{12} in BCF is on the order of $-0.52 \text{ m}^3 \text{s}^{-3}$. The minima of both BCB and OC2 are approximately 23% less intense, on the order of $0.40 \text{ m}^3 \text{s}^{-3}$. These trends agree with expectations as the lower region of a turbine wake recovers toward the undisturbed boundary layer much more slowly than the top region; the global supply of momentum to the wake area can only come from above the canopy.

5. CONCLUSIONS

The experiment presented here investigates flow associated with positions immediately upstream and downstream of wind turbines in Cartesian and row-offset array configurations. In the experiment, power measurements were collected via torque sensors fixed to turbine model nacelles. Measurements of the flow were collected with SPIV yielding velocity and turbulence statistics that show clearly defined wakes and dynamics generated by strong gradients and the presence of solid bodies. The wakes show statistically similar behavior in dynamics and structure to other turbine array experiments include some references?

For the same configurations, the power coefficient, c_p , is shown to be about 22% of the maximum by the fourth row. In contrast, the row-offset configuration does much to mitigate the perceived underperformance of installations in the array. The power coefficient of the exit row in the offset configurations was approximately 8% greater than entrance rows, likely an effect of the particular rotor blades used in the experiment performing better at slightly reduced speeds or more uniform inflow velocities.

Dynamics and turbulence in the wake of each turbine depend greatly on both the depth of the wind turbine in the array as well as the arrangement of turbines. The row-offset configuration of turbines grants greater spacing between turbines in a streamwise sense without significantly altering the density of turbines per unit area of land. The Reynolds shear stresses reach maximum values several rows within the array, confirming the presentations of Chamorro and Porté-Agel.^{13,14} In the aforementioned results, the stress $-\bar{u}\bar{v}$ reaches maximum and minimum values approximately 15% less extreme in the entrance row than in the exit row wakes for either array configuration.

High levels of turbulence and strong gradients of velocity in areas associated with the rotor blades contribute to a loss of energy available to following turbines. In the wakes, the in-plane production of turbulence kinetic energy, P_{12} , is greatly driven by the strong gradient of the mean streamwise velocity near the tips of the rotor. P_{12} is shown to be some 25% less in the fourth row of the base configuration than in the row-offset case. Thus, one can expect an increased turbulence production from a turbine driven by a flow more closely resembling the approach flow conditions. This result implies that individual turbines in the row-offset configuration of the array produced more turbulence than in the Cartesian configuration. However, when the additional streamwise spacing is taken into consideration, wakes still have more room to recover and subsequent turbines have a cleaner inflow profile.

The calculated flux of kinetic energy in wind turbine wakes confirms the entrainment of energy downward from the flow above the turbine canopy. This behavior is shown in the mean wall-normal velocity, V , where distinct downward trends in the region of the wakes trailing the top-tip of the rotors. The net flux of kinetic energy is toward the vertical center of the wake, where the momentum deficit is greatest. The research presented here demonstrates that at the fourth row of turbines in an array, high-momentum fluid is approximately 7.5% more effectively entrained from above and into the turbine canopy in row-offset configurations. This augmentation is likely due to the differences in development of the turbine canopy layer between the array configurations.

To further explore the particular effects of turbine position and array configuration on the production of power, low-dimensional descriptions of turbulence and the flux of kinetic energy made through the proper orthogonal decomposition

lend insight to the structure and relative energy content of different turbulence scales. Behavior of the wakes as seen through the flux of kinetic energy and turbulence production are compared according to the modes used in reconstructions. Results from the application of the proper orthogonal decomposition and low-dimensional representations of turbulence quantities are discussed in *Part II* of the paper.

ACKNOWLEDGEMENTS

The authors are grateful to the National Science Foundation's brige program for funding this research (project no. ECCS-1032647). The authors also acknowledge Mr. Dominic DeLucia for carrying out the torque measurements for the arrays.

REFERENCES

1. Ainslie JF. Calculating the flowfield in the wake of wind turbines. *Journal of Wind Engineering and Industrial Aerodynamics* 1988; **27**: 213–224.
2. Vermeer LJ, Sorensen JN, Crespo A. Wind turbine wake aerodynamics. *Progress in Aerospace Sciences* 2003; **39**: 457–510.
3. Whale J, Papadopoulos KH, Anderson CG, Helmis CG, Skyner DJ. A study of the near wake structure of a wind turbine comparing measurements from laboratory and full-scale experiments. *Solar Energy* 1996; **56**(6): 621–633.
4. Snel H. Review of aerodynamics for wind turbines. *Wind Energy* 2003; **6**(3): 203–211. [Online]. Available: <http://dx.doi.org/10.1002/we.97> [Accessed date: August 30, 2012].
5. Barthelmie R, Rathmann O, Frandsen S, Hansen K, Politis E, Prospathopoulos J, Rados K, Cabezon D, Schlez W, Phillips J, Neubert A, Schepers JG, van der Pijl SP. Modelling and measurements of wakes in large wind farms. *Journal of Physics: Conference series* 2007; **75**(1): 012049.
6. Crespo A, Hernandez J, Frandsen S. Survey of modelling methods for wind turbine wakes and wind farms. *Wind Energy* 1999; **2**: 1–24.
7. Frandsen S, Barthelmie R, Pryor S, Tahmann O, Larsen S, Hojstrup J. Analytical modelling of wind speed deficit in large offshore wind farms. *Wind Energy* 2006; **9**: 39–53.
8. Rathmann O, Frandsen S, Barthelmie R. Wake modeling for intermediate and large wind farms, 2007.
9. Meyers J, Meneveau C. Optimal turbine spacing in fully developed wind-farm boundary layers. *Wind Energy* 2012; **15**: 305–317.
10. Chamorro LP, Porte-Agel F. A wind-tunnel investigation of wind-turbine wakes: boundary-layer turbulence effects. *Boundary Layer Metrology* 2009; **132**: 129–149.
11. Wu Y-T, Porté-Agel F. Atmospheric turbulence effects on wind-turbine wakes: an LES study. *Energies* 2012; **5**(12): 5340–5362.
12. Ebert PR, Wood DH. The near wake of a model horizontal-axis wind turbine—I. experimental arrangements and initial results. *Renewable Energy* 1997; **12**(3): 225–243.
13. Chamorro LP, Arndt REA, Sotiropoulos F. Turbulent flow properties around a staggered wind farm. *Boundary Layer Metrology* 2011; **141**: 349–367.
14. Chamorro LP, Porte-Agel F. Turbulent flow inside and above a wind farm: a wind-tunnel study. *Energies* 2011; **4**: 1916–1936.
15. Cal RB, Lebron J, Castillo L, Kang HS, Meneveau C. Experimental study of the horizontally averaged flow structure in a model wind-turbine array boundary layer. *Journal of Renewable and Sustainable Energy* 2010; **2**(013106): 1–25.
16. Hamilton N, Kang HS, Meneveau C, Cal RB. Statistical analysis of kinetic energy entrainment in a model wind turbine array boundary layer. *Journal of Renewable and Sustainable Energy* 2012; **4**(6): 063105–063105.
17. Kang HS, Meneveau C. Direct mechanical torque sensor for model wind turbines, 2010.
18. Burton T, Jenkins N, Sharpe D, Bossanyi E. *Wind Energy Handbook*. John Wiley & Sons: Chichester, West Sussex, England, 2011.
19. Ragheb M, Ragheb AM. *Wind Turbines Theory-the Betz Equation and Optimal Rotor Tip Speed Ratio* (Carriiveau R, ed.) InTech: Rijeka, Croatia, 2011. pp. 19–37, Fundamental and Advanced Topics in Wind Power.
20. Cook NJ. Wind-tunnel simulaion of the adiabatic atmospheric boundary layer by roughness, barrier and mixing-device methods. *Journal of Industrial Aerodynamics* 1978; **3**: 157–176.

21. Counihan J. An improved method of simulating an atmospheric boundary layer in a wind tunnel. *Atmospheric Environment* 1969; **3**: 197–214.
22. Irwin H. The design of spires for wind simulation. *Journal of Wind Engineering and Industrial Aerodynamics* 1981; **7**(3): 361–366.
23. Stull RB. *An Introduction to Boundary Layer Meteorology*. Springer: Kluwer Academic. Dordrecht, Netherlands, 1988.
24. Zhang W, Markfort CD, Porté-Agel F. Near-wake flow structure downwind of a wind turbine in a turbulent boundary layer. *Experiments in fluids* 2012; **52**(5): 1219–1235.
25. Espa   G, Aubrun S, Loyer S, Devinant P. Spatial study of the wake meandering using modelled wind turbines in a wind tunnel. *Wind Energy* 2011; **14**(7): 923–937.
26. Espa   G, Aubrun S, Loyer S, Devinant P. Wind tunnel study of the wake meandering downstream of a modelled wind turbine as an effect of large scale turbulent eddies. *Journal of Wind Engineering and Industrial Aerodynamics* 2012; **101**: 24–33.
27. Saranyasoontorn K, Manuel L. Low-dimensional representations of inflow turbulence and wind turbine response using proper orthogonal decomposition. *ASME* 2005; **127**(4): 553.
28. Frandsen S, Thogersen ML. Integrated fatigue loading for wind turbines in wind farms by combining ambient turbulence and wakes. *Wind Engineering* 1999; **23**(6): 327–340.
29. Chamorro LP, Arndt REA, Sotiropoulos F. Reynolds number dependence of turbulence statistics in the wake of wind turbines. *Wind Energy* 2012; **15**(5): 733–742. [Online]. Available: <http://dx.doi.org/10.1002/we.501> [Accessed date: October 13, 2012].